Engineering Geology 112 (2010) 53–67

Contents lists available at ScienceDirect

Engineering Geology

journal homepage: www.elsevier.com/locate/enggeo

# Kinematic behaviour and velocity characteristics of a complex deep-seated crystalline rockslide system in relation to its interaction with a dam reservoir

C. Zangerl [a,*], E. Eberhardt [b], S. Perzlmaier [c]

[a] alpS — Centre of Natural Hazard and Risk Management, Grabenweg 3, A-6020 Innsbruck, Austria
[b] Geological Engineering/Earth and Ocean Sciences, University of British Columbia, Vancouver, BC, Canada V6T 1Z4
[c] TIWAG — Tiroler Wasserkraft AG, Eduard-Wallnöfer-Platz 2, A-6020 Innsbruck, Austria

ARTICLE INFO

*Article history:*
Received 28 April 2009
Received in revised form 13 January 2010
Accepted 15 January 2010
Available online 25 January 2010

*Keywords:*
Rockslides
Crystalline rock mass
Deformation monitoring
Dam reservoir
Hydromechanical interactions

ABSTRACT

This paper presents the geometry, kinematics and temporal deformation characteristics of a deep-seated rockslide system, the "Hochmais–Atemkopf", situated above the Gepatsch dam reservoir in Northern Tyrol, Austria. Results from surface and subsurface geological investigations and deformation monitoring indicate that the Hochmais–Atemkopf rockslide system involves several sliding masses, one on top of the other, characterized by different velocity characteristics with displacements being greater for the shallower slide bodies. During the initial impounding phases of the Gepatsch reservoir, uplift forces beneath the foot of the slope led to the activation of one of these shallower slide bodies, moving it more than 10 m downslope in 2 years. After continuous deceleration of the sliding mass, the deformation rates reduced to about 2 to 4 cm per year. These were found to show seasonal fluctuations that correlated with reservoir levels and drawdown conditions, with induced slope accelerations peaking when reservoir levels were at their lowest. This suggests, in part, a controlling mechanism based on seepage forces where reservoir drawdown drives the episodic rockslide deformation behaviour. Together, the data and analyses presented demonstrate the importance of integrating detailed geology and monitoring data to derive a basic understanding of the kinematics and controlling mechanisms of a deep-seated rockslide system in advance of undertaking comprehensive numerical modelling.



## 1. Introduction

Deep-seated rockslides in deeply incised alpine valleys are a common hazard that threatens communities and critical infrastructure such as highways, railways and dams. If they fail rapidly and develop into far-reaching runout rock flows (Abele, 1974; Azzoni et al., 1992; Brideau et al., 2005), their destructive capability is immense. Fortunately, many of these deep-seated rockslides, especially those observed in mica-rich crystalline rock masses (e.g. mica schists, phyllites), do not fail suddenly or reach high velocities (e.g. Noverraz, 1996; Crosta and Agliardi, 2002; Helmstetter et al., 2004; Brückl et al., 2006; Bonzanigo et al., 2007; Zangerl et al., 2007). Instead, they move at speeds of several centimetres per year (or even less) and show evidence of episodic accelerations, sometimes reaching alarming levels but then subsiding to non-critical levels. The pre-conditioning factors and triggering mechanisms contributing to these episodes are diverse: heavy rainfall, snow melt, fluctuation of reservoir levels at the foot of the slope, changes in the slope's equilibrium state due to strength degradation, antecedent deformation processes, changes in the material behaviour within the sliding zone, erosion along the foot of the slope, etc. (Zangerl et al., 2007).

A peculiarity of these slopes is their ability to decelerate after an acceleration period and return to low velocities. Precise surface deformation data demonstrate that these slopes often show a relatively linear "creep" trend comprised of intermittent phases of acceleration and deceleration (Weidner, 2000; Crosta and Agliardi, 2002; Helmstetter et al., 2004; Bonzanigo et al., 2007; Zangerl et al., 2007). To assess and understand the temporal deformation characteristics of a deep-seated rock slope instability, which is imperative for assessing the hazard it poses or to set early warning alarm thresholds, data are required regarding the slide geometry, geology, kinematics, and the temporally varying slope velocity trends. Monitoring with sufficient temporal resolution is essential for the latter. Furthermore, the mechanical behaviour of the basal sliding zones, together with any secondary shear zones, needs to be understood as these zones are where most of the slope deformation localizes. Such rupture zones contain breccias and/or gouges (i.e. material that is formed through cataclasis and fragmentation of the rock during deformation and shearing), and which possesses soil-like mechanical properties. In some cases, rockslide rupture surfaces have been observed to develop through the reactivation of favourably orientated pre-existing brittle

* Corresponding author. Postal address: alpS — Centre for Natural Hazard and Risk Management, Grabenweg 3, A-6020 Innsbruck, Austria. Tel.: +43 512 392929 14; fax: +43 512 392929 39.
*E-mail address:* zangerl@alps-gmbh.com (C. Zangerl).

0013-7952/$ – see front matter © 2010 Elsevier B.V. All rights reserved.
doi:10.1016/j.enggeo.2010.01.001

fault zones of tectonic origin. The tectonically formed fault breccias or gouges in these cases act to partly or fully reduce the shear strength along the sliding zone.

Less frequently, case studies have been reported where a heavily fractured rock slab has slid onto glacial till, talus and/or alluvial deposits located along the lower valley walls, suggesting slip magnitudes of several hundred metres (Lauffer et al., 1967; Leobacher and Liegler, 1998). In such cases, a sliding zone may evolve along the contact between the sliding mass and Quaternary deposits, and if deformation is dispersed and continuous, also within the glacial deposits (Lauffer et al., 1967).

This paper reports the findings of historical and new investigations of a deep-seated rockslide system characterized by several individual sliding masses situated above the Gepatsch dam reservoir in Northern Tyrol, Austria, the Hochmais–Atemkopf. The paper focuses on analyses of surface and subsurface deformation measurements integrated with geological data sets to develop a geometrical and kinematic model of the rockslide system. Deformation measurements are evaluated in terms of the internal deformation of the slide, its time-dependent activity and possible triggers and stabilization factors. In addition, data on the structure and deformation of an internally active sliding zone in glacial till and talus deposits is presented. The analyses documented herein provide the basis for further work involving the development of hydromechanically coupled numerical creep models for the rockslide system (Schneider-Muntau et al., 2006a,b).

## 2. Geological and structural setting

The Hochmais–Atemkopf rockslide system covers an area of 2.82 km$^2$; the height of the slope is about 1000 m. Numerous investigations and monitoring of the slope have been carried out due to the presence of a hydroelectric dam reservoir (Lauffer et al., 1967). The reservoir has a volume capacity of 140 million m$^3$ and submerges the lower 100 m of the slope (Fig. 1).

The study site is situated within the poly-metamorphic Ötztal–Stubai crystalline complex of the Austroalpine units which is composed mainly of E–W striking layers of paragneisses, mica schist and orthogneisses (Hammer, 1923; Hoinkes et al., 1994). After deglaciation several slope instabilities developed in this region, likely as a result of stress redistribution due to valley steepening and deepening within the lower strength paragneisses and schists. The Hochmais–Atemkopf rockslide system is located within a heavily foliated and folded paragneissic rock unit. The orientation of the

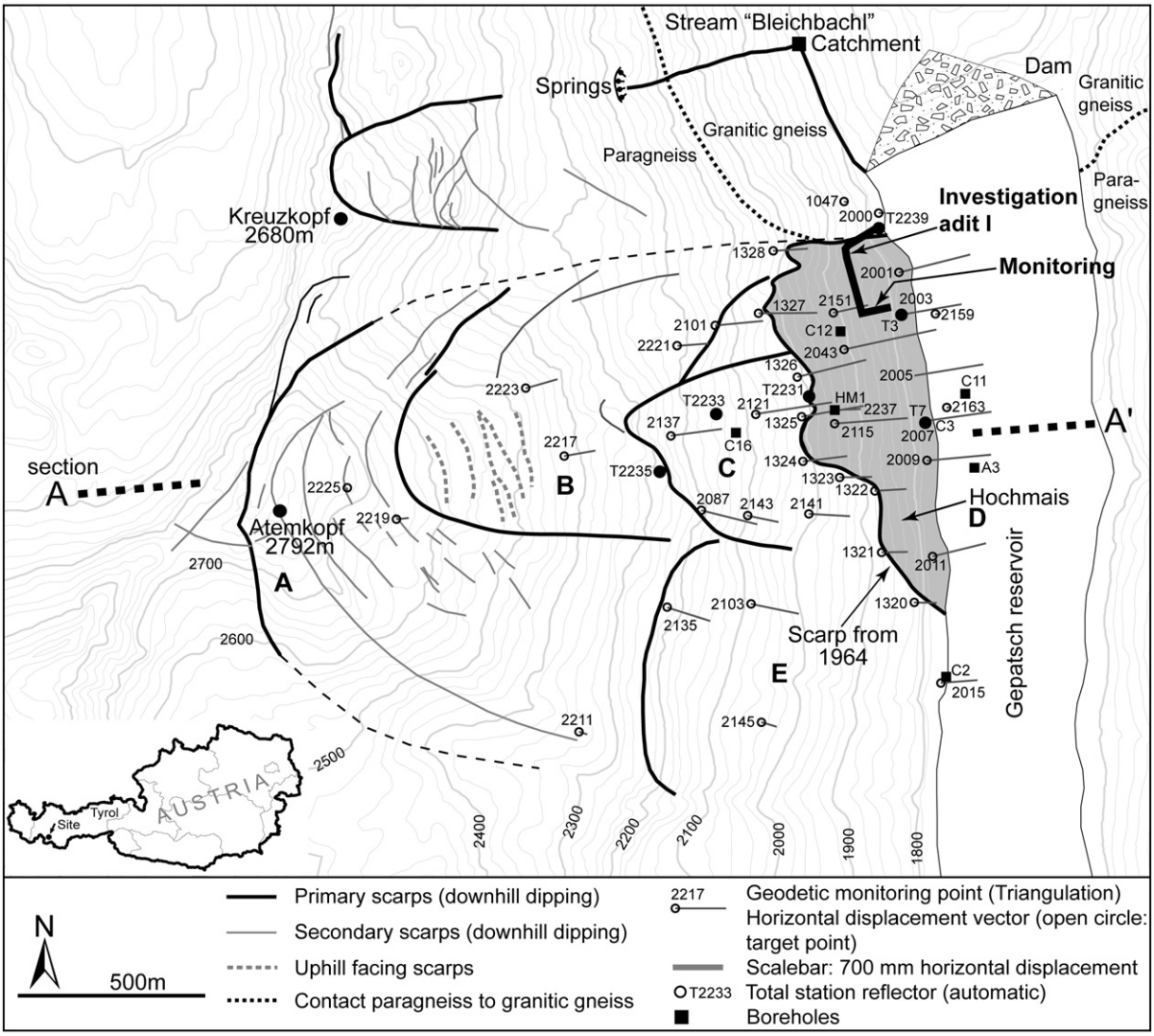


**Fig. 1.** Map of primary and secondary scarps along the Hochmais–Atemkopf rockslide system, showing the individual rockslide masses A to E, the displacement vectors obtained from periodic triangulation measurements, the automatic total station monitoring points, the location of the boreholes HM1, C16, C3, C2, C11, C12 and A3 (only boreholes relevant for the paper were included) and the location of the investigation adit I that passes from the stable bedrock into the Hochmais slab, the location of the spring "Bleichbachl" and the lithological contact between paragneisses and granitic gneisses.

foliation dips to the west and south, a direction that does not align to promote slope failure or accommodate a persistent failure plane (Fig. 2a, Brückl et al., 2004). Instead, intensive structural field mapping in the area shows that the formation of the Hochmais–Atemkopf rockslide system is largely influenced by pre-existing meso-scale discontinuities (i.e. tensile joints and shear fractures) aligned subperpendicular to the foliation. Although structural mapping showed a varied distribution of fracture orientations (Fig. 2), a densely spaced fracture set (#1 in Fig. 2, Table 1) orientated subparallel to the eastward dipping slope was identified as being a dominant set. In addition, two steeply inclined sets striking NNW–SSE and E–W (#2 and #3 in Fig. 2, respectively) and a medium to flatly dipping set to the NW (#4) were observed (Fig. 2). The mean normal spacing of these three joint sets ranges between 1.5 and 2 m (Table 1). Fracture sets #1 and #2 generate a mechanical rock mass anisotropy that favours the progressive failure and formation of coherent sliding surfaces subparallel to the slope. This same failure mechanism and promotion of shear surface formation was also observed for the neighbouring Kreuzkopf rockslide north of the Atemkopf (see Fig. 1), where the same structural environment exists. Again, a close relationship between the shape of the main sliding zone and the meso-scale fracture pattern was observed which is presented in detail in Zangerl and Prager (2008). Of special interest with respect to the study of the Hochmais–Atemkopf rockslide system, and deep-seated rockslides in crystalline rock in general, is that the neighbouring Kreuzkopf rockslide represents a displaced mountain ridge where the basal rupture zone is laterally well exposed. This rare field situation enables the study of geomorphological and geological features along the rockslide profile, including the interrelationship between the geometry of the sliding zone and the discontinuity network, both near the scarp at the top of the rockslide and laterally along most of the slide's southern flank (Fig. 1).

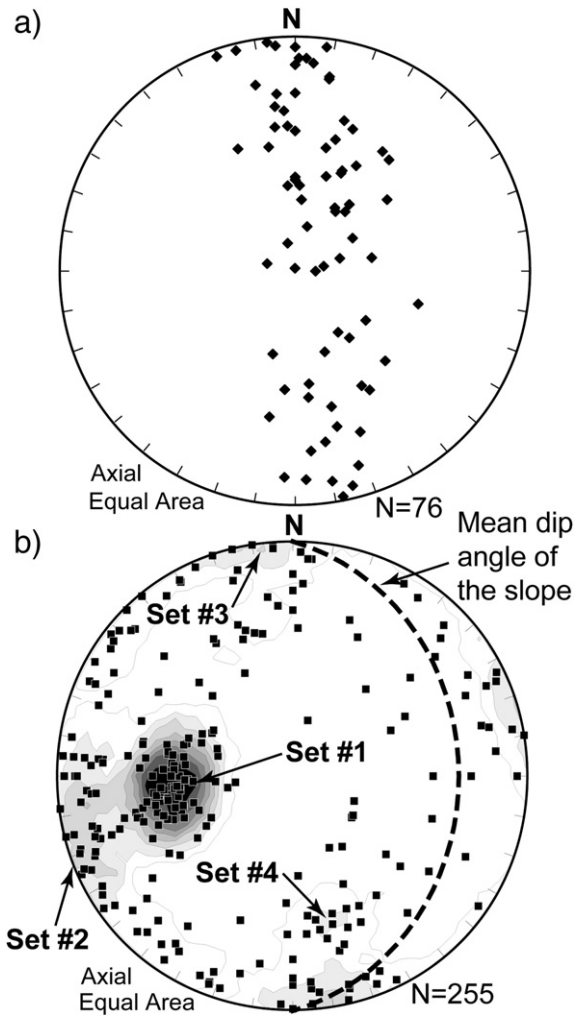


**Fig. 2.** Pole plots (lower hemisphere) of dip direction and dip angle (a) of foliation planes and (b) of meso-scale fractures including the great circle of the mean slope dip angle.

**Table 1**
Mean orientation and spacing of discontinuities in paragneisses at the Hochmais–Atemkopf rockslide system.

| Set number | Number of data | Mean dip direction (°) | Mean dip angle (°) | Mean normal spacing (m) |
|---|---|---|---|---|
| Set #1 | 93 | 90 | 45 | 0.5 |
| Set #2 | 66 | 67 | 88 | 1.5 |
| Set #3 | 64 | 166 | 83 | 1.5 |
| Set #4 | 32 | 338 | 49 | 2 |

## 3. Investigation methods

In order to develop an integrated kinematic, geological, and geotechnical model of the rockslide system, several *in-situ* investigations were performed. These include: a) surface mapping of the slide boundaries, geology (lithologies, discontinuities, etc.) and geomorphological features (downhill- and uphill facing scarps, tension cracks, etc.); b) subsurface mapping through investigation adits and boreholes (up to 200 m in depth) to obtain details regarding the depths of the different active and non-active sliding zones, degree of fracturing of the sliding masses and the ground water situation; c) seismic investigations to determine the shape of the sliding mass and its boundary with the stable bedrock (Brückl et al., 2004); and d) airborne laser scanning (LiDAR) to map geomorphological features of the rockslide system.

The presence of the Gepatsch hydroelectric reservoir also provides the study with a unique long-term monitoring data set that covers a period of more than 40 years. The monitoring system includes several independently working surface and subsurface displacement measurement devices, several of which serve as part of an early warning system. Deformation data, integrated with the geological and geotechnical data, were used to develop a kinematic model of the rockslide, with further integration of the hydrological data being used to provide valuable insights into the episodic acceleration/deceleration behaviour of the slide. The deformation monitoring data sets include those from: a) a continuously operating wire-line extensometer installed in an investigation adit (see adit I in Fig. 1) spanning an active portion of the sliding mass and its boundary with the stable bedrock (resolution 1 mm); b) a periodically measured geodetic triangulation network based on 39 target points distributed across the rockslide system (accuracy $<\pm 3$ cm, Fig. 1); c) an automatic total station device which monitors five reflectors on a 4 to 5 h time interval (T3, T7, T2231, T2233, and T2235; Fig. 1, single measurement accuracy $<\pm 2$ cm), d) periodic total station measurements targeting across the main scarp at the top of the Atemkopf (accuracy $<\pm$ 2 mm); e) periodic levelling campaigns along the investigation adit and the quayside to measure vertical displacements (standard deviation $<0.8$ mm/km); f) satellite Interferometric Synthetic Aperture Radar (InSAR) to determine the surface deformation field (Rott et al., 1999); and g) borehole inclinometer measurements in borehole HM1 (Fig. 1) to identify and locate active sliding zones and to determine the degree of internal deformation of the sliding masses (Tentschert, 1998).

## 4. Geometry and kinematics of the rockslide system

Geological and geomorphological observations (e.g. Figs. 1 and 3), were used together with borehole core logs, mapping data from the

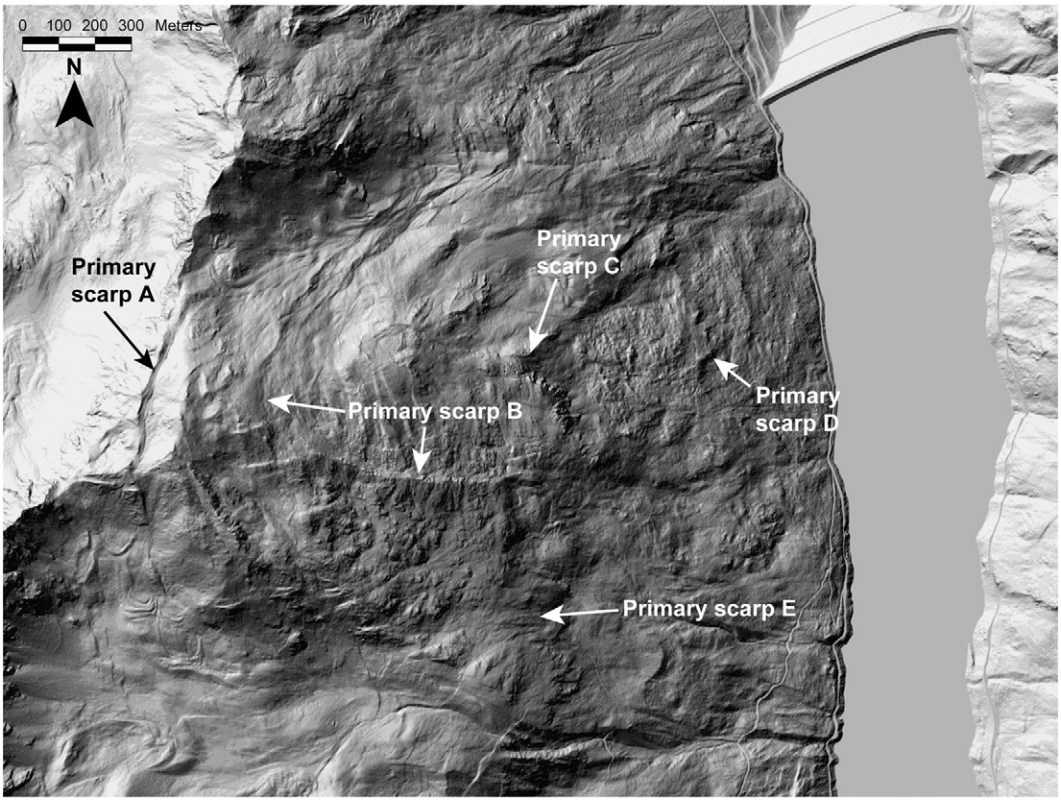


**Fig. 3.** Airborne laser scanning map (LiDAR based hillshade) of the study site showing main scarps of the individual rockslide masses A to E. LiDAR data show a position accuracy of ± 15 cm, an elevation accuracy of ± 30 cm, and a data density of 1 point per 1 $m^2$ below 2000 m, and 1 point per 4 $m^2$ above 2000 m elevation, respectively (Amt der Tiroler Landesregierung, Geoinformation).

investigation adits, seismic data, and point-, line- and surface area deformation measurements to develop a kinematic model of the Hochmais–Atemkopf rockslide system. These show that the rockslide can be subdivided into 5 main sliding bodies (labelled A to E in Figs. 1, 3 and 4), which are bounded by well-defined back scarps and lateral boundaries (Figs. 1 and 3). In addition, the rupture surface for sliding mass D could be clearly identified in the borehole inclinometer and adit wire-line extensometer and levelling measurements, respectively (Figs. 1 and 4). The shape and depth of the sliding zones of the other slide bodies were further defined by seismic investigations, borehole core logs, surface deformation measurements and geological data.

Data from the geodetic triangulation network were analysed to develop a surface deformation map of the displacement vectors for these different bodies (Fig. 1). The total displacement vector represents the resultant vector obtained from the horizontal N–S, the horizontal E–W and vertical displacement component. Using data

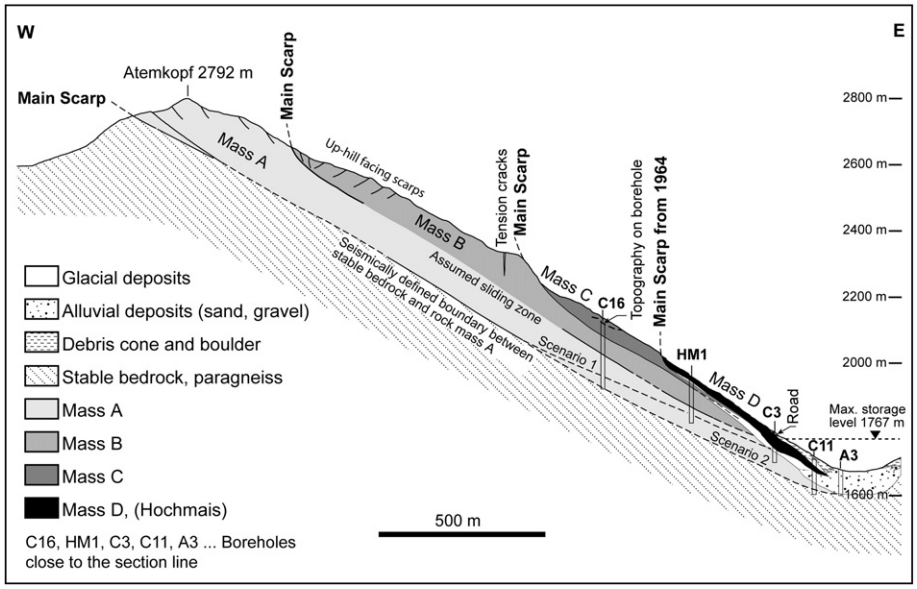


**Fig. 4.** Geological W–E cross section (see Fig. 1 for location A–A′) showing four individual rock mass bodies bounded by primary scarps with different degrees of activity. The Hochmais slab (mass D) is shaded black. In addition the location of boreholes near the cross section is shown.

collected over several measuring campaigns (between 1965/66 and 2002), dip angles of these vectors, and there changes with time if any, were compared to the projections of the dip angles of the sliding surfaces for each of the 5 slide masses. This comparison was used to provide further insights into the kinematic behaviour of each component of the rockslide system, a summary of which is provided in Table 2. Only those target points for which a high coefficient of determination exists (i.e. $>0.95$), were used. The results from this comparison for each of the 5 slide masses are reported in detail below.

### 4.1. Slide mass A

The lower boundary of the rockslide system, coinciding with that for slide mass A, was determined by means of seismic data (Brückl et al., 2004), borehole core logs and geomorphological observations (Fig. 4). The back scarp to slide mass A is clearly evident and appears at an elevation of about 2700 m west of and incorporating the Atemkopf mountain peak (Figs. 1, 3 and 5). The distance between the northern and southern lateral boundaries spans about 1500 m. Based on seismic investigations a maximum thickness of the rockslide system of about 220 m was obtained. A total volume of 290 million $m^3$ (0.29 $km^3$) was determined (i.e. including slide bodies A to E) using a digital elevation model of the surface topography and the seismically determined basal separation boundary (Brückl et al., 2004).

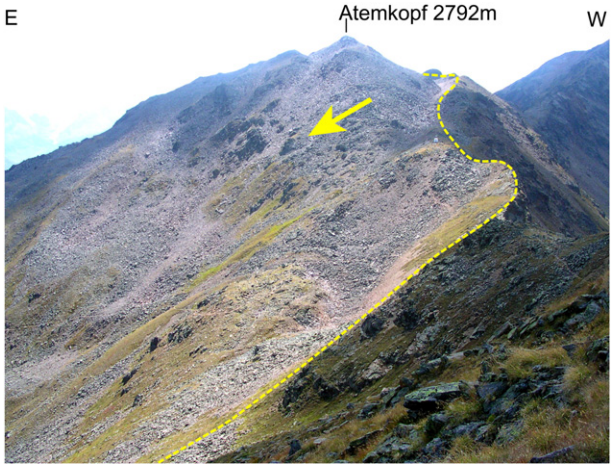


**Fig. 5.** View of primary back scarp of the Atemkopf rockslide system from the north.

At the Atemkopf's summit, the main scarp appears as a deep trench with clear indications of slip displacements of mass A (Figs. 4 and 5). Total displacements of up to 30 m on the basal slide surface can be measured here. This establishes the presence of a distinct sliding zone

**Table 2**
Comparison of the mean dip angle obtained from displacement vectors of triangulation and total station targets and projected sliding zones.

| Slide mass | Target number | Measurement period | Total displacement vector (m) | Mean dip angle of total displacement vector[a] (°) | Coefficient of determination ($R^2$) | Estimated mean dip angle of the main sliding zone (°) |
|---|---|---|---|---|---|---|
| A | 2225 | 10.07.1984–27.08.2002 | 0.069 | – | – | 31 |
| | 2219 | 15.08.1966–27.08.2002 | 0.223 | 39.4 | 0.956 | |
| | 2211 | 15.08.1966–27.08.2002 | 0.153 | 30.3 | 0.855 | |
| B | 2217 | 15.08.1966–27.08.2002 | 0.615 | 45.5 | 0.965 | 32 |
| | 2223 | 15.08.1966–27.08.2002 | 0.617 | 41.6 | 0.988 | |
| | 2221 | 15.08.1966–27.08.2002 | 0.530 | 36.2 | 0.981 | |
| | 2101 | 15.05.1966 – 27.08.2002 | 0.765 | 28.3 | 0.996 | |
| | T2235 | 15.01.1999–15.07.2004 | 0.092 | 43.9 | 0.824 | |
| | 1328 | 15.05.1974–27.08.2002 | 0.532 | 24.5 | 0.981 | |
| C | 1321 | 15.05.1974–27.08.2002 | 0.389 | 27.1 | 0.979 | 32 |
| | 1322 | 15.05.1974–27.08.2002 | 0.463 | 22.8 | 0.953 | |
| | 1323 | 15.05.1974–27.08.2002 | 0.475 | 21.7 | 0.997 | |
| | 1324 | 15.05.1974–27.08.2002 | 0.693 | 30.4 | 0.995 | |
| | 1325 | 15.05.1974–27.08.2002 | 0.982 | 26.7 | 0.994 | |
| | 1326 | 15.05.1974–27.08.2002 | 1.070 | 22.1 | 0.988 | |
| | 1327 | 15.05.1974–27.08.2002 | 0.944 | 30.1 | 0.999 | |
| | 2121 | 15.05.1966–27.08.2002 | 1.252 | 30.3 | 0.998 | |
| | 2137 | 15.11.1965–27.08.2002 | 0.883 | 35.0 | 0.993 | |
| | 2087 | 15.11.1965–27.08.2002 | 1.064 | 40.9 | 0.997 | |
| | 2141 | 15.11.1965–27.08.2002 | 0.614 | 21.5 | 0.993 | |
| | 2143 | 15.11.1965–27.08.2002 | 0.550 | 37.1 | 0.995 | |
| | T2233 | 15.01.1999–15.07.2004 | 0.167 | 36.5 | 0.948 | |
| | T2231 | 15.01.1999 – 15.07.2004 | 0.219 | 27.7 | 0.968 | |
| D | 2001 | 15.05.1966–27.08.2002 | 1.158 | 27.0 | 0.990 | 32 |
| | 2003 | 15.05.1966–28.05.2002 | 1.048 | 31.9 | 0.997 | |
| | 2005 | 01.05.1966–27.08.2002 | 1.170 | 33.5 | 1.000 | |
| | 2007 | 01.05.1966–28.05.2002 | 1.165 | 34.7 | 0.998 | |
| | 2009 | 15.05.1966–27.08.2002 | 1.049 | 31.0 | 0.996 | |
| | 2011 | 15.05.1966–28.05.2002 | 0.869 | 28.5 | 0.997 | |
| | 2043 | 15.05.1966–27.08.2002 | 1.558 | 31.7 | 0.998 | |
| | 2115 | 15.05.1966–03.10.2002 | 1.558 | 27.4 | 0.992 | |
| | 2151 | 15.08.1986–27.08.2002 | 0.585 | 31.8 | 0.995 | |
| | 2237 | 01.09.1993 – 03.10.2002 | 0.410 | 23.8 | 0.977 | |
| | 2159 | 13.06.1997–15.05.2002 | 0.084 | 14.6 | 0.994 | |
| | 2163 | 13.06.1997–15.05.2002 | 0.075 | 19.2 | 0.998 | |
| | T3 | 15.01.1999 – 15.07.2004 | 0.147 | 38.5 | 0.982 | |
| | T7 | 15.01.1999–15.07.2004 | 0.157 | 38.2 | 0.953 | |
| E | 1320 | 15.05.1974–27.08.2002 | 0.319 | 15.5 | 0.955 | 32 |
| | 2015 | 15.05.1966–28.05.2002 | 0.557 | 23.0 | 0.993 | |
| | 2103 | 15.05.1966–27.08.2002 | 0.747 | 35.0 | 0.953 | |
| | 2135 | 15.11.1965–27.08.2002 | 0.727 | 31.1 | 0.987 | |
| | 2145 | 15.11.1965–27.08.2002 | 0.256 | 30.4 | 0.984 | |

[a] Determined by a linear least-square regression analyses.

beneath mass A, at least in the upper part of the slope, along which significant downhill displacements have occurred. However, geodetic measurements performed from the valley bottom to a triangulation target (measuring point 2225, see Fig. 1) near the top of the slope show no slope movements since monitoring began in 1984. Between 4 to 6 mm/year has been measured lower down on mass A (points 2211 and 2219), but these velocities are attributed to movements arising from their close proximity to the back scarps of masses B and E, where movement of the lower slide blocks accommodate movements and opening of extensional cracks higher up the slope. A recently installed high accuracy geodetic survey network targeting reflectors positioned across the Atemkopf, combining stable points outside and points on mass A, has shown no signs of activity of mass A in the scarp region since measurements began in 2004.

The location where the main rupture surface daylights at the slope toe, or if it daylights, is not exactly known as the lower slopes are covered by valley sediments (glacial, alluvial, colluvial, etc.). Analyses of high-precision levelling data measured along the 390 m long investigation adit I show no sign of a second active sliding zone that could represent the main rupture surface of mass A near the valley bottom. In fact, levelling data indicate only one active sliding zone coinciding with the lower boundary of sliding mass D (Fig. 6). The portal of the investigation adit is located outside of the Hochmais–Atemkopf rockslide system in a competent Augengneissic rock mass. This is confirmed by a stable levelling point close to the adit portal. In addition, geomorphological observations and triangulation points (i.e. 1047 and 2000) outside the rock slide system show negligible movements and provide constraints for the boundary between the rock slide system and stable rock (Fig. 1). In the adit several steeply inclined E–W striking fault zones were observed where one of them could represent the main northern boundary of mass A. If this is the case mass A would be inactive because there are no signs of movement along the adit accept those from the lower boundary of mass D. Interpretations based on the above noted data sources suggest two different scenarios: either the basal rupture surface coalesces into a splay root together with the other slide surfaces intersecting the valley at the toe of the slope (scenario 1 in Fig. 4), or the basal rupture surface is deeper, dipping below the valley floor (scenario 2 in Fig. 4). In the first case, the lower boundary of the slide system would daylight between 1600 and 1750 m elevation into the valley at the toe of the slope. Kinematically, the entire slide system would be free to slide in a translational manner as the toe would be unconstrained. In contrast, a lower projection for the surface would require a more complex toe deformation mechanism for kinematic release. This question has important implications with respect to the hazard posed by the rockslide and is further discussed in the Discussion.

### 4.2. Slide mass B

Sliding mass B daylights in the middle to upper part of the slope and is defined on the basis of geomorphological features (i.e. active scarps), geodetic measurements and synthetic aperture radar interferometry (Rott et al., 1999). The southern boundary separates the highly fractured, fragmented rock mass of sliding mass B with the less intensively deformed mass A (Fig. 3). Relative comparisons of displacement rates calculated from the geodetic monitoring data show points located on mass B (Table 2, Fig. 1) as being more active than mass A but less active than the adjacent mass C (compare Fig. 7a and b). Coloured aerial photographs and airborne LiDAR derived digital elevation models (i.e. hillshade relief maps) show that the main scarp of mass B lies within a topographic hollow between the Kreuzkopf and Atemkopf ridges (Figs. 1 and 3). The geometrical intersection between the topography and the main scarp suggests a considerable thickness of the sliding mass in the range of 70 to 100 m.

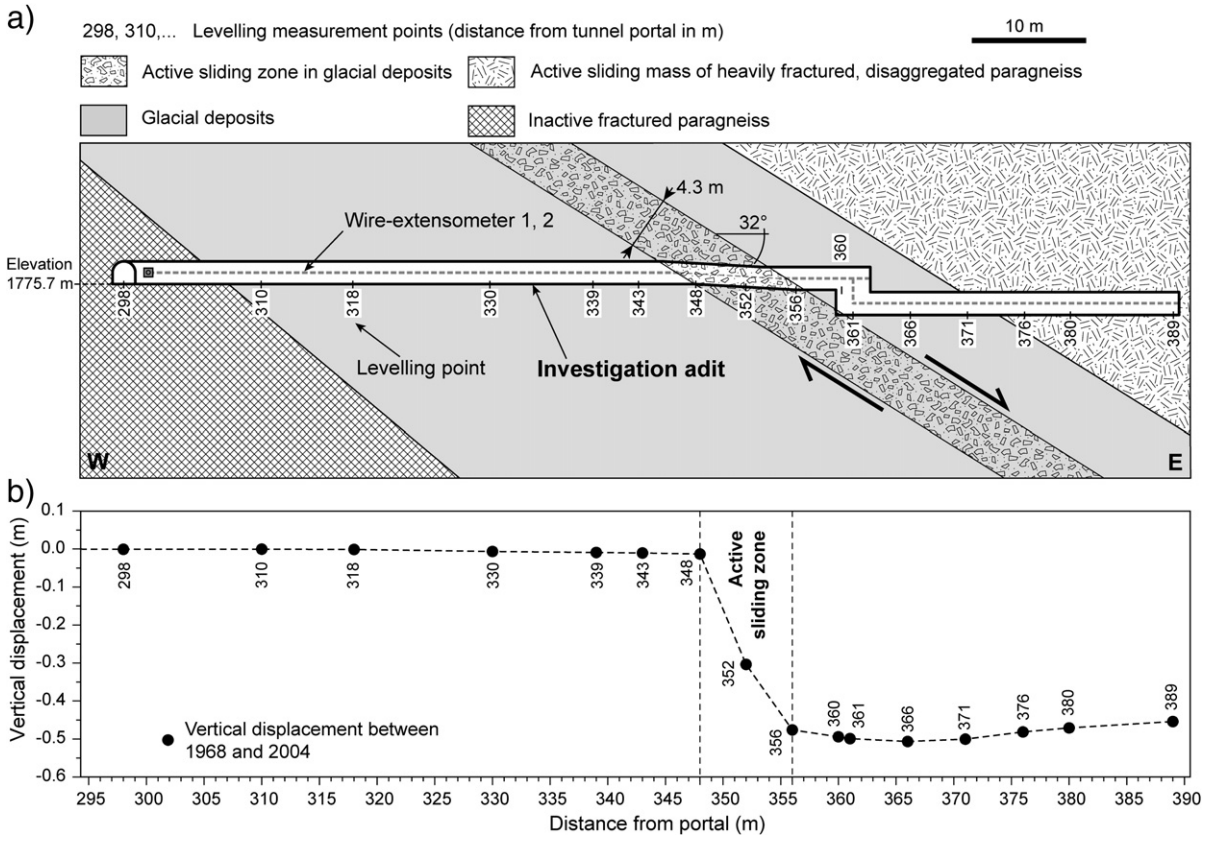


**Fig. 6.** a) Cross section through the investigation adit I showing the thickness and dip of the active sliding zone, the glacial till deposits, the active sliding mass, the stable bedrock, the set-up of the wire-extensometer and the location of individual levelling points. b) Vertical displacement measured on levelling points between the period 1968 to 2004 (location of levelling points in the adit are shown above, the accuracy of the levelling measurements is within ±1 mm).

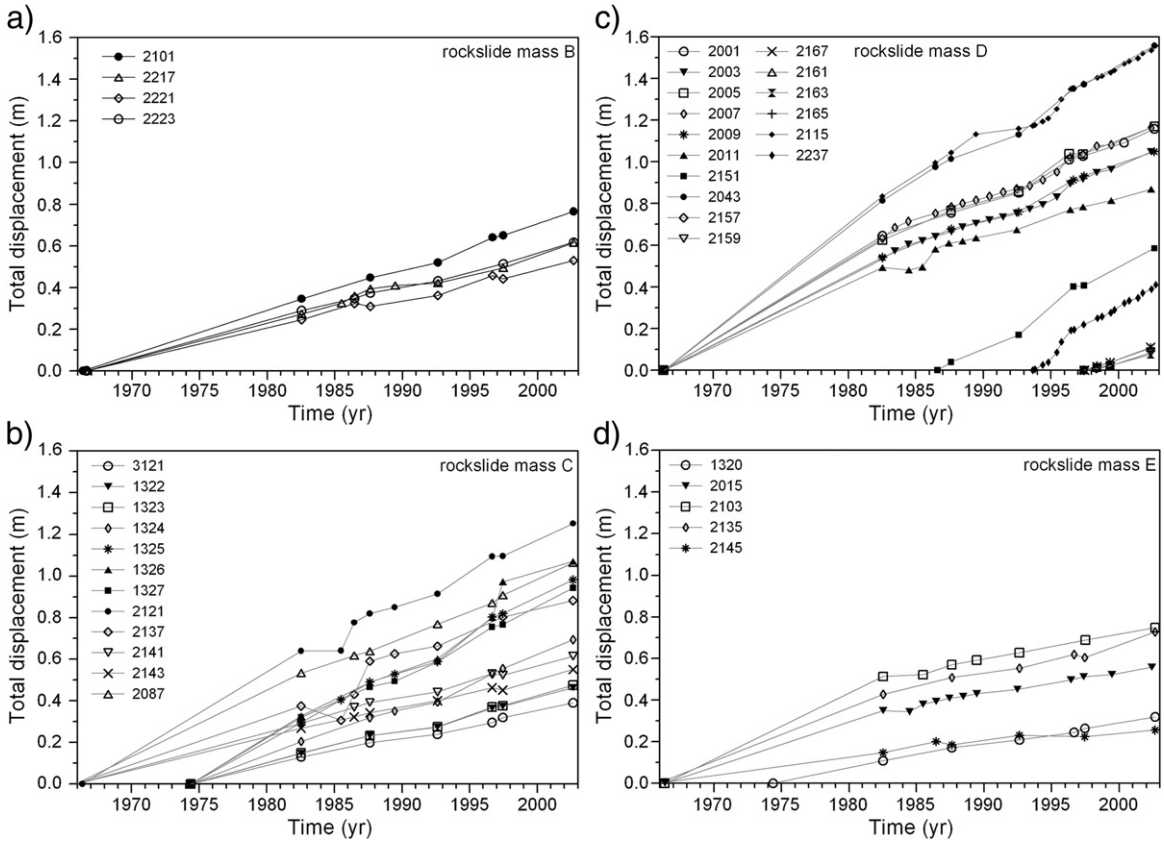


**Fig. 7.** Total displacement in metres versus time for triangulation targets on a) sliding mass B, b) sliding mass C, c) sliding mass D and d) sliding mass E.

This geomorphological projection is supported by core logs from borehole C16, where an 81 m interval containing zones of increased fracture density, intensive rock fragmentation and uncemented gouges and kakirites are associated with this part of the sliding mass.

The surficial morphology of sliding mass B is characterized by secondary downhill scarps, uphill facing scarps and tension cracks (Figs. 1, 3 and 4). The occurrence of uphill facing scarps and tension cracks suggest some evidence for extensional straining of mass B. The mean dip angles of the total displacement vectors associated with each monitoring point were derived using a linear least-square regression analysis of the data spanning the different periodic measurement campaigns. In the upper part of mass B, dip angles of 42° and 46° were found for points 2223 and 2217, respectively (Table 2). For the automatic total station reflector T2235, a dip angle of 44° was calculated (Fig. 1). The two points 2221 and 2101, located just above the main scarp of sliding mass C, show dip angles of 36° and 28°, respectively.

The relatively high dip angles observed for sliding mass B are likely the result of secondary downhill- and uphill facing scarp development and extensional strains within the sliding mass itself. The interaction between these extensional strains and the pre-existing rock mass fracture network would act to induce secondary, uphill facing scarps during slip, which in turn would locally increase the dip angle of the displacement vectors (Zangerl and Prager, 2008). These geomorphological features are numerous in mass B, and are observable in both air photo and LiDAR imagery (Fig. 3).

### 4.3. Lower slide bodies (masses C and D)

Originally, sliding masses C and D (the latter referred to locally as the Hochmais) formed a single sliding body, which post-glacially experienced a sliding event in which the rock mass slid several hundred metres on top of the blanket of glacial and talus deposits that at that time covered the lower valley flanks. This large amount of downhill displacement induced rock mass fracturing and disruption and led to a blocky debris-like sliding mass. Evidence for this detachment can be found in the borehole cores drilled through slide mass D (boreholes C12, and HM1 in Fig. 1), where glacial till deposits several metres thick were intersected below the fragmented rock corresponding to the lower boundary of mass D. Similarly, during the excavation of the investigation adit I, a 60 m zone of glacial till was intersected, also beneath the base of the disturbed, blocky rock of mass D (Fig. 4). Radiocarbon dating of wood pieces obtained from valley fill deposits near the lower boundary of sliding mass D constrain the age of this sliding event to 9310 calibrated years before present (Prager et al. 2008). The wood samples analysed by radio carbon dating methods originated from cores of the borehole C11 at a depth of 37 m (Figs. 1 and 4). Several thousand years later, during the first impounding of the Gepatsch reservoir in 1964, acceleration of the lower part of the slope led to the separation of sliding masses C and D. Thus a new scarp i.e. the main scarp of mass D (Fig. 1) and a primary sliding zone within the soil deposits was formed (Fig. 4).

Sliding mass C is characterized by large internal rock mass deformation and significant disturbance (extension cracks, block toppling, etc.). Interpretation and extrapolation of core logs from boreholes C16 and HM1, in combination with surface mapping data, suggest that sliding mass C possibly reaches depths of 40 to 50 m. Geodetic monitoring points on sliding mass C show a dip angle variation of the total displacement vectors between 22 and 41° (Table 2), with a trend of increasing dip angle with increasing elevation. This suggests a translational mode of sliding for most of mass C, with mixed rotational and translational modes closer to its back scarp in relation to extensional strains, internal shearing and secondary scarp development.

Given the more recent activity of sliding mass D (referred to locally as the Hochmais), and the more than 10 m of slip that occurred during the first reservoir impounding, considerable effort was spent on investigating

and trying to understand and predict its behaviour and stability. This included the aforementioned boreholes, investigation adits, surface mapping, geodetic monitoring, wire-line extensometer and levelling surveys. The volume of sliding mass D is estimated to reach more than 13 million $m^3$, which is based on an area of 440,000 $m^2$ and mean thickness of 30 m, with a maximum thickness of 50 m estimated from levelling data along the investigation adit. In the vicinity of borehole HM1, inclinometer measurements indicate a depth of the base of sliding mass D at about 16 m (Fig. 8). The displacement vectors on sliding mass D measured from survey targets set up along a road (elevation 1778 to 1795 m) dip from 27 to 35° (points 2001 to 2011), and further up the slope they dip from 24 to 32° (targets 2151, 2043, 2237, and 2115). Several of these records are shown in Fig. 9. Together, their dip angles correspond to that of the sliding surface extrapolated for mass D from the borehole and investigation adit data (Fig. 4) suggesting a translational mode of movement. In contrast, two triangulation points located below the road show dip angles of 15° and 19° (respectively, targets 2159 at 1726 m and 2163 at 1730 m, Fig. 1). This indicates that near the valley bottom, the slope parallel displacement vectors rotate to a subhorizontal orientation, suggesting that the slide surface daylights near the valley bottom.

In the lower part of the slope, the subsurface boundaries between sliding masses B, C and D are difficult to separate (Fig. 4). Inclinometer data from borehole HM1, located at 1942 m elevation (Fig. 1), clearly shows the lower boundary of sliding mass D as defined by an active sliding zone between 15 and 17 m depth (Fig. 8). Below this active zone, deformations occur to a depth of 88 m suggesting en block movements. Geodetic measurements of the inclinometer head suggest that the inclinometer does not extent into stable bedrock; the shear along the active sliding zone is considerably less than the total surface displacement. This makes it difficult to draw further conclusions regarding the location of the sliding zones for masses A to C. Core logs from borehole HM1 show a layer of soil-like material at a depth of 25.2 to 26.3 m (Fig. 10), which is interpreted to be the boundary between masses B and C. However, the inclinometer in HM1 does not show any evidence for active sliding along this zone, at least since its installation. This could simply be that this zone has not been recently active, or that both masses (B and C) are moving with the same velocity. If this is correct, mass C must coalesce into mass D (Fig. 4). New subsurface investigations are currently being planned to help resolve this question.

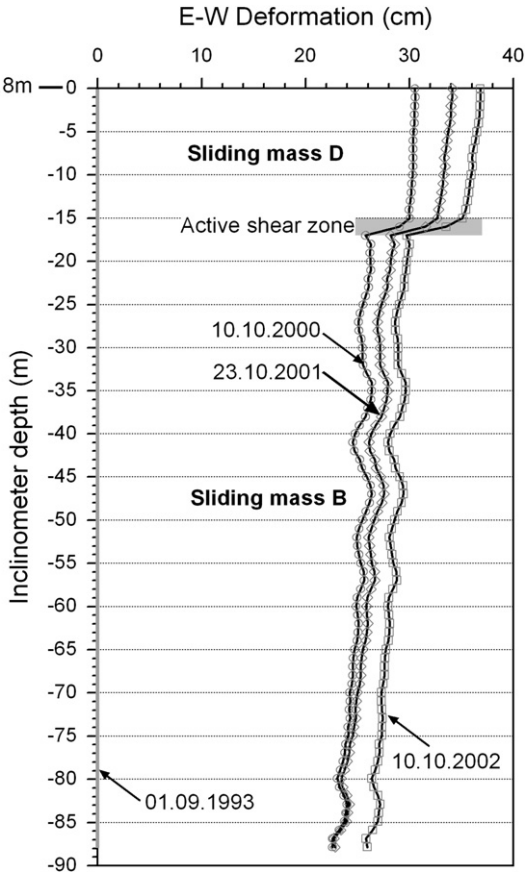


**Fig. 8.** Cumulative deformation plot for the HM1 inclinometer as measured over several repeat surveys between 1993 and 2002. See Fig. 1 for location of the borehole HM1.

### 4.4. Slide mass E

The geometry and kinematic deformation mechanism of slide mass E is less well defined than the others. Based on geological core logs (borehole C2), the base of sliding mass E can be located at a depth of 72 m. However, this borehole (drilled in 1964) was not installed with an inclinometer system and therefore the thickness of mass E cannot be confidently established. The dip angles of the total displacement vectors in the lower part of mass E for the targets 1320 and 2015 is 16 and 23°, respectively (Table 2). This increases to angles between 30 and 35° in the upper part of the slope (targets 2103, 2135, and 2145).

## 5. Sliding mechanisms and internal deformation

Being the more active slide mass, and therefore drawing the most attention, the investigation efforts to date have primarily concentrated on sliding mass D (the Hochmais). The available data sets for analysis include, on surface, periodic geodetic triangulation surveys, automatic total station measurements, levelling measurements, airborne LiDAR data, and geomorphological and geological mapping data. At depth, data are available from instrumented boreholes (inclinometer) and investigation adits (extensometer, levelling).

During the initial infilling of the reservoir a new sliding zone initiated within the buried glacial till deposits that were overridden during prehistoric rockslide activity (Fig. 4). This sliding zone was targeted at depth by the investigation adit I (Figs. 1 and 6). Along the adit I, several levelling points were fixed and an automatic wire-line extensometer was positioned across the sliding zone (Fig. 6). The levelling data provided information on the vertical component of displacement, the wire-line extensometer measured the horizontal component, and from both data sets the dip angle of the displacement vector at the base of slide mass D could be resolved through a regression analysis. From this analysis, a dip angle of 32° with a high coefficient of determination of $R = 0.999$ was found (Fig. 11). As shown in Fig. 6, the sliding zone's lower boundary coincides with levelling point 348 and the upper boundary at point 356. Levelling point 352 is located between these two, within the heavily sheared material, and indicates an equally dispersed deformation across the sliding zone rather than a sharp, localized slip along a distinct shear surface. From the horizontal thickness of the sliding zone and the dip angle of the displacement vector, a true thickness of 4.3 m was determined for the sliding zone in this area.

Displacement vectors on surface above the investigation adit (see Fig. 1) show dip angles between 31° and 35° (Fig. 9a to f). Surface displacement vectors were determined from long-term geodetic measurements since 1965/66. Comparison of the annual mean velocities obtained from triangulation targets on surface above the investigation adit (targets 2001, 2003, 2005 and 2007) to those recorded by the wire-line extensometer in the adit at the base of the slide mass show values that are only 1 to 3 mm per year higher. A comparison of levelling data from surveys along the road and from within the investigation adit show only minor differences in vertical displacement (time interval 1982 to 2004). As previously noted, inclinometer measurements along borehole HM1 show the active

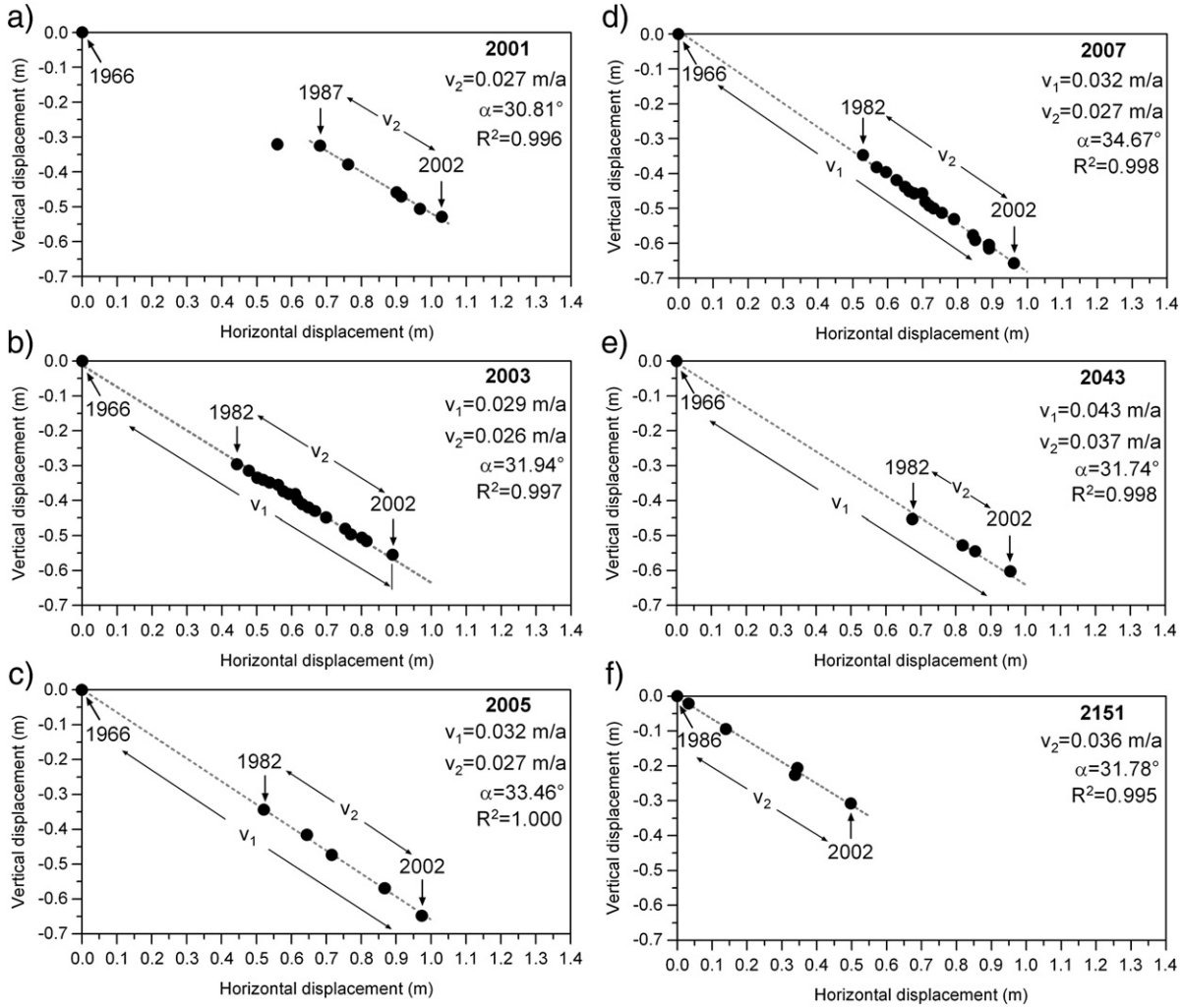


**Fig. 9.** Horizontal versus vertical displacements in the surrounding of the investigation adit I representing the dip angle of the total displacement vector over time of a) target 2001, b) target 2003, c) target 2005, d) target 2007, e) target 2043 and f) target 2151 ($v_1$..., mean annual velocity obtained from periods 1966 to 2002, $v_2$... mean annual velocity obtained from periods 1982 to 2002, 1987 to 2002 for fig. a, 1986 to 2002 for fig. f), $\alpha$...dip angle of total displacement vector, $R^2$...coefficient of determination).

basal sliding zone of slab D at a depth between 15 and 17 m (Figs. 8 and 10). The sliding mass above (i.e. the Hochmais slab) is characterized by a low magnitude of internal deformation. This is observable in the inclinometer measurements, the triangulation and levelling measurements on surface, and measurements within the investigation adit. This means that slope deformation is dominated by plastic yield and strain localisation within the several metres thick active sliding zone and furthermore slope stability is highly influenced by the temporal mechanical behaviour of this sliding zone.

## 6. Temporal variations and coupled hydromechanical behaviour

### *6.1. Velocity trends of the Hochmais sliding mass during the initial reservoir impoundment*

Initial impoundment of the reservoir began in July 1964, with monitoring and the first measured movements of mass D beginning in September 1964. Fig. 12 shows the downslope vertical displacements measured during impoundment and its temporal relationship with the reservoir levels (modified after Lauffer et al., 1967). Lauffer et al. (1967) assumed that movement of sliding mass D initiated when the reservoir level reached 1670 m; i.e., a water column of about 10 m above the valley floor. The subsequent displacements during the first impoundment (between July 1964 and March 1965) reached 7.4 m horizontally and 5.0 m vertically. Based on the mean of five geodetic targets located at an elevation of 1800 m, a total displacement vector of 8.9 m with a dip angle of 34° was resolved. The data in Fig. 12 indicate that during the first phase, most of the vertical displacement occurred after the peak reservoir level of about 1719 m was reached. Approximately 2.7 of the total 5 m, or 54%, occurred during the 43 days the reservoir level was held constant. Subsequent lowering of the water level then led to stabilization of the slope.

For the second reservoir impoundment (April 1965 to April 1966), horizontal displacements of 3.5 m, vertical displacements of 2.4 m, and a total displacement of 4.2 m with a dip angle of 34° were measured. The slope movements didn't begin until the highest reservoir level of the first impounding phase was exceeded, with most of the displacements occurring during a sudden acceleration event (July 1965) where the downward vertical velocity reached 19 cm/day (Fig. 12; Lauffer et al., 1967). Previous to this, negligible slope movements were detected during the second impoundment. In order to avoid further slope accelerations, the reservoir level was lowered 5 m, which in turn led to a rapid decrease in slope velocity. The infilling procedure was subsequently continued, during which only minor additional vertical displacements developed (Fig. 12). A similar trend of negligible activity continued into the third impounding phase to a reservoir level of 1767 m. Overall, the three impounding phases were followed by a considerable reduction in the slope velocities to a few centimetres per year with the reservoir at its normal operating level.

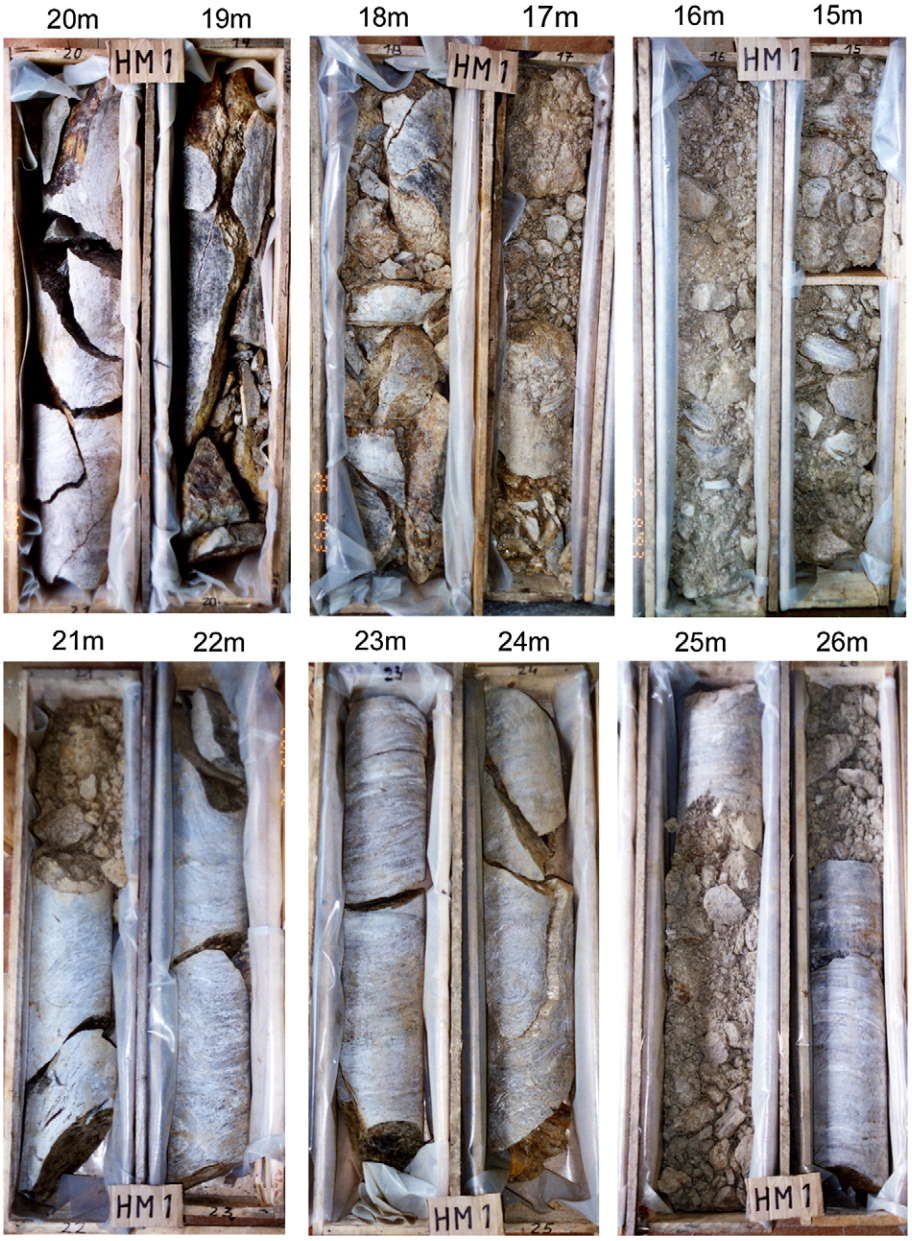


**Fig. 10.** Photos of the HM1 borehole cores from depth 15 to 26 m.

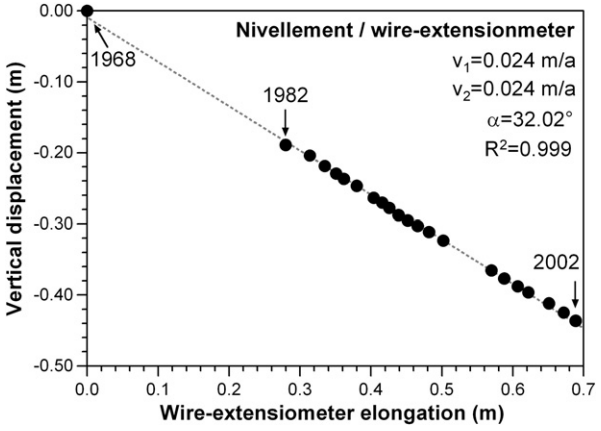


**Fig. 11.** Calculation of the total displacement vector dip angle on the base of sliding mass D based on regression analysis from periodic levelling and continuous wire-extensometer measurements ($v_1$... mean annual velocity obtained from time interval 1968 to 2002, and $v_2$... from 1982 to 2002).

### 6.2. Impact of the reservoir on the activity of the Hochmais sliding mass

As noted above, the annual deformation rate of sliding mass D (Hochmais) has averaged a few centimetres per year following impoundment. The wire-line extensometer installed in the investigation adit across the active sliding zone beneath mass D (Fig. 6) enabled the sampling of horizontal displacements with a high resolution of 1 mm. Based on the midpoint rule, the cumulative horizontal displacement curve was numerically differentiated over time (Fig. 13a). The dip angle of the resulting velocity vector (32°) was found to be equal to the total displacement vector on surface (31–35°) and constant over time (Figs. 9 and 11), allowing it to be used to establish statistical relationships between slope velocity and hydrological triggering events.

Analyses of the slope velocity data show that the annual velocity differs between high and low activity by up to a factor of 100, ranging between 0.01 mm/day and 1 mm/day (Fig. 13a). Every year an acceleration phase begins between January and March and lasts into the summer. However, this trend does not easily correlate with the

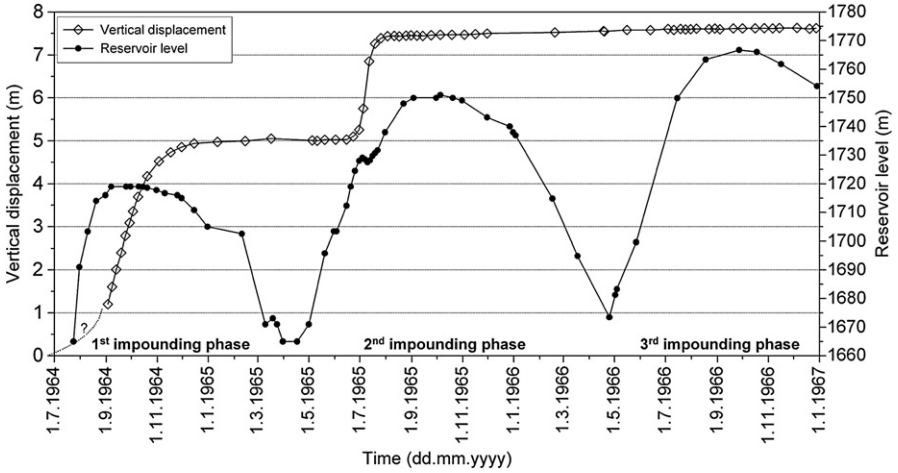


**Fig. 12.** Temporal relationship between initial reservoir impoundment and vertical displacements of slide mass D measured along the road.

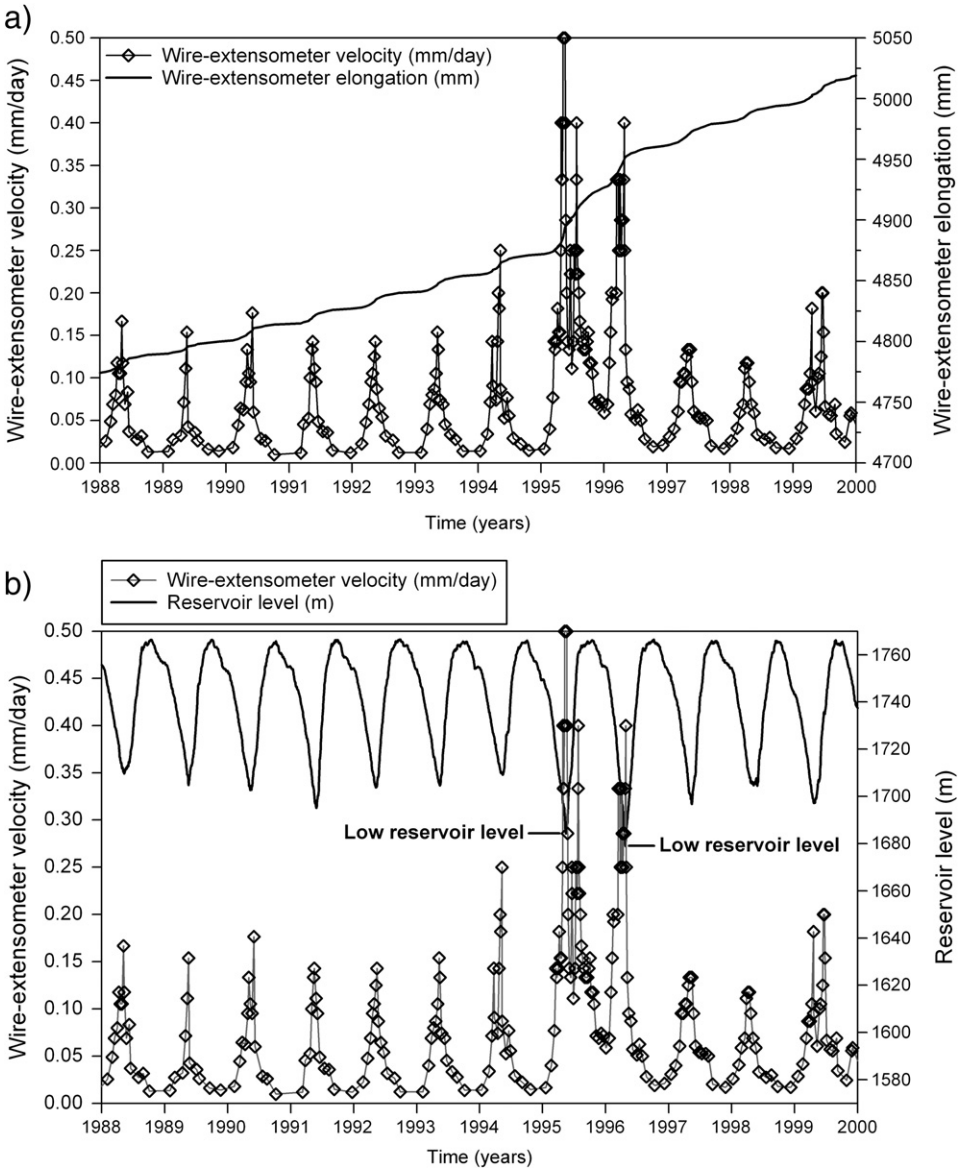


**Fig. 13.** a) Measured elongation of the wire-extensometer and the differentiated horizontal velocities of sliding mass D (Hochmais slab), b) Time-dependent variation of slope velocity and reservoir level.

seasonal climatic record. In order to better understand the trigger for the acceleration phases, available hydrological and hydrogeological data sets were analysed to more accurately establish the correlation. No significant water inflows were measured in the investigation adit which could be monitored and analysed with regard to the groundwater situation. Instead, the most reliable data involved flow rate measurements from a continuously monitored spring (several measurements per day) located north of the Atemkopf–Hochmais rockslide system (see Fig. 1). These could be analysed to establish a temporal relationship between rainfall, snow melt and the slope activity.

The spring line above the Bleichbachl stream (Fig. 1) can be found at an elevation of about 2180 m on an eastwards facing slope above the dam. The catchment of the stream is located at about 1800 m and from there the water is drained along a closed channel into the reservoir. The flow rates were monitored at the boundary of the reservoir. Given that the flow rate monitoring device was installed 380 m below the spring, both groundwater and surface runoff water (i.e. rainfall, snowmelt) mix into the stream (and the measured flows). This added flow component serves as a temporal indicator when snow melting or precipitation accounts for groundwater recharge.

Observations based on 10 years of monitoring (1989 to 1999) show that the flow rate of the spring increases each year around the middle of April to early May. Fig. 14 shows a typical flow rate record measured over a period of a year. This increase in April agrees with flow rate data measured in a second investigation adit, termed adit S3, below the Nasserein rockslide several hundred meters to the south of the Hochmais–Atemkopf rockslide system (see Lauffer et al., 1967; Tentschert, 1998). There the flow rate of groundwater drained into the adit also shows flow rate increases each year in late April in response to snow melt and precipitation.

Examination of the extensometer data of movements across the sliding zone below mass D (Fig. 14) typically shows a phase of acceleration that only partly correlates to the increased snow melt and precipitation in April. Furthermore, the annual initiation of accelerated velocities actually begins much earlier in the year around late January and early March. This means that the phase of slope acceleration occurs during a period where neither precipitation in the form of rainfall nor snow melting is relevant. This points to annual fluctuations in the reservoir level as a possible control on the slope accelerations. To establish this, long-term velocity and reservoir level data were analysed. Comparison of the reservoir level data with slope velocity measurements from the wire-line extensometer shows an excellent temporal agreement between the slope velocity and reservoir level (Fig. 13b). It can be shown that low reservoir levels occurring typically in the months from January to May coincide with the acceleration phase which lasts into May (Fig. 14). Slope velocities peak when the reservoir levels reach their low point and subside when the reservoir levels are at their highest (Figs. 13b and 14). This correlation was especially evident during the periods 1995–1996 and 1996–1997, where very low levels in the reservoir were reached and higher slope velocities were observed. During refilling of the reservoir in autumn and early winter, the slope velocities decrease and reach their minimum (<0.02 mm/day).

Fig. 15 shows the results of a statistical analysis, in the form of a scatter plot, that suggest a general trend where higher slope velocities coincide with lower reservoir levels, and vice versa. Several data points from the years 1975, 1987 and 1995 are located in the area of high reservoir levels combined with relatively high slope velocities. Whereas for the year 1975 a possible trigger is not clear, the anomaly from 1987 can be explained by extraordinary precipitation events. The high velocities during the high reservoir level period in the year 1995 may be the result of an extraordinary acceleration phase of about 1 mm/day which initiated during spring time when reservoir drawdown was exceptionally low. Evers (2006), who performed both linear and non-linear regression analyses found a statistical correlation between the reservoir level and slope velocity and thus confirmed our observations. He observed that a non-linear quadratic

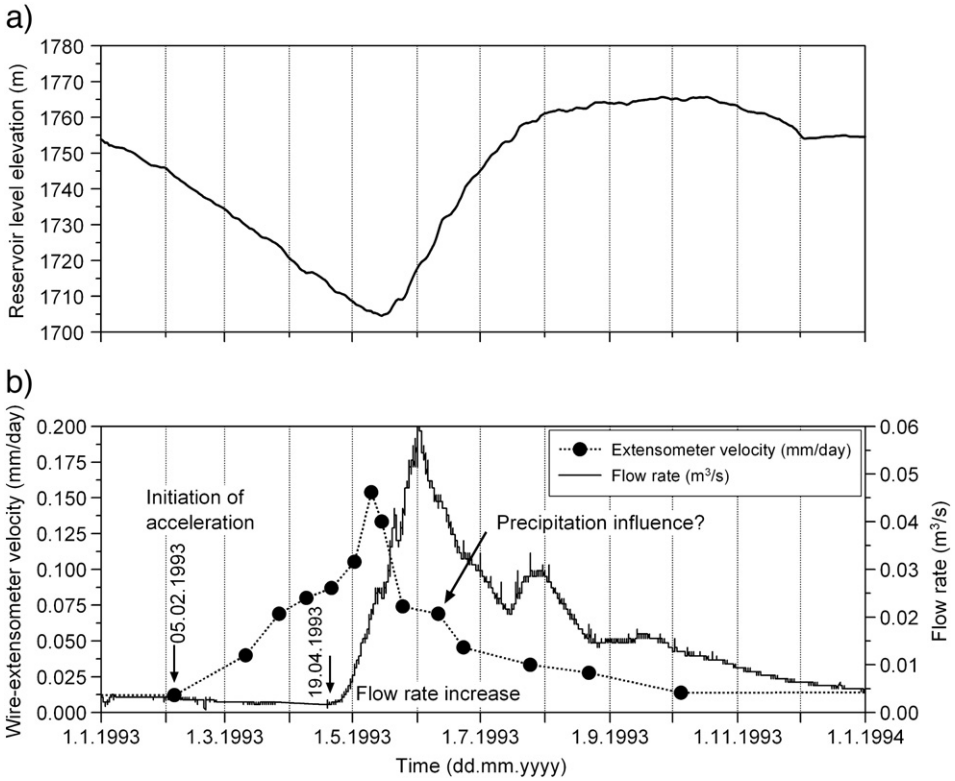


**Fig. 14.** a) Variation of the reservoir level for the period 01.01.1993 to 01.01.1994. b) Variation of the wire-extensometer velocity and the flow rate of the Bleichbachl for the same time interval.

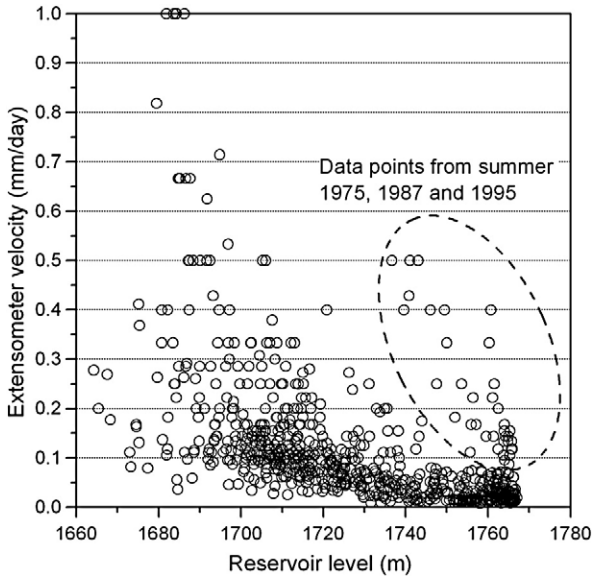


**Fig. 15.** Correlation between the reservoir level and the wire-extensometer velocity measurements.

function provided the best fit to the data with a coefficient of determination of $R=0.75$. Fig. 16 shows the relationship between slope velocity and reservoir drawdown velocity. At first this data appears to suggest an influence of the velocity of reservoir drawdown on slope velocities. However, a more detailed inspection of Fig. 16 shows that high slope velocities were only reached when the reservoir level was low. This means that drawdown velocity does not directly correlate with slope velocity, but indirectly as drawdown velocities will increase as reservoir levels decrease. In other words, the v-shape profile of the reservoir must be considered as its volume sharply decreases as the reservoir level decreases, thus contributing to an increasing drawdown velocity. As a result, the actual reservoir level provides a better control on the correlation.

Together, the data indicates that the changing reservoir level is the dominant mechanism responsible for the intermittent accelerating slope behaviour. The effect of precipitation and snow melt on slope

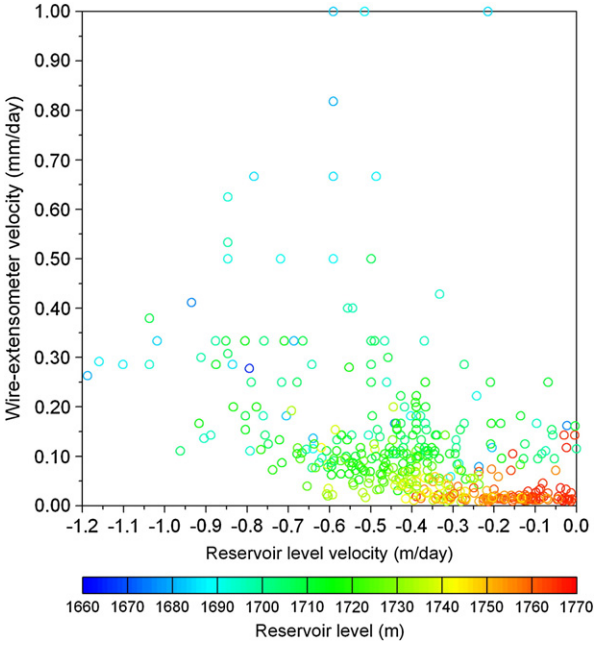


**Fig. 16.** Correlation between reservoir level velocity and wire-extensometer based slope velocity. The colour of the open circles indicates the reservoir level.

acceleration was found to be significantly weaker. For example, in mid-July 1987 the wire-line extensometer measured a significant acceleration event of up to 0.5 mm/day that temporally coincided with extraordinarily high precipitation rates during June and July. During this period the reservoir level was continuously rising, with the exception of two minor drawdown phases: the first from 20th May to 3rd June with a water level depletion of 3.3 m, and the second from 22nd to 24th June characterized by a very small drawdown of 0.35 m. Based on observations from earlier and subsequent operating years, the observed acceleration phase cannot be explained by these small decreases in reservoir level therefore pointing to a precipitation trigger instead.

### 6.3. Overall velocity trends since reservoir impoundment

The velocity trends of the other sliding masses (A, B, C and E) vary considerably in relation to the reservoir impoundment. In order to investigate these, triangulation measurements were compared. The reference measurement of the triangulation network was completed after the maximum level of the 2nd impounding phase was reached (Nov 1965), or in some cases after the 2nd infilling and depletion cycle (May 1966). In either case, monitoring didn't begin until after the large displacements of sliding mass D had already halted (Fig. 7).

As already noted, the data indicates that no evidence of slope movements for sliding mass A have been recorded since monitoring began.

Measurements between 1966 and 2002 show sliding mass B as moving at velocities of 1.5 to 2.1 ($\pm$0.14) cm per year. The highly linear trends of these velocities for the periods 1966 to 2002 suggest that the reservoir impoundment had no effect on the movements of the deeper mass B (Fig. 7a).

Displacements recorded between 1982 and 2002 for sliding mass C show that it is moving downslope with a mean annual velocity between 1.1 and 3.7 ($\pm$0.25) cm per year. Additional determinations based on datasets for the periods 1965/66 to 2002 and 1974 to 2002 show a similar trend. Spatially, triangulation targets located on sliding mass C close to the main scarp of sliding mass D (i.e. 1321 to 1326, Figs. 1 and 7b) show a continuous increase in the annual mean velocity from south to north with the highest velocity measured at point 1326. At point 1327, which is located further north, the velocity is lower again. The highest velocities for sliding mass C were obtained in the middle, lower part of the mass and range from 3.1 to 3.7 ($\pm$0.25) cm/year. Generally, surface velocities are lower near the main sliding mass boundaries for mass C. The large variation in measured velocities across sliding mass C may be the result of spatially variable internal strain within the sliding mass, or individual block movements. Internal strains in a sliding mass may produce a highly fractured/fragmented rock mass and an undulating surface topography. The spatially variable internal-strain hypothesis is supported by high-resolution LiDAR mapping, in which irregular, highly disturbed surfaces can be seen relative to the much smoother surfaces seen for rockslide masses A and B (Fig. 3). Velocity plots for individual geodetic targets on sliding mass C show only a minor interaction with the reservoir following impounding, and a slight deceleration over time (Fig. 7b).

Periodic triangulation surveys of mass D between 1966 to 2002 show a mean displacement rate of 2.4 to 4.3 ($\pm$0.14) cm/year (for example see Figs. 9a to f and 7c). However, when the same data set is analysed with respect to the time interval 1997 to 2002, a considerably slower annual surface velocity in the range of 1.7 to 3.6 ($\pm$0.60) cm/year is found. For comparison, velocities obtained for the period 1999 to 2004 for the total station reflectors T3 and T7 (Fig. 1) show 2.7 and 2.9 ($\pm$0.36) cm/year, respectively. These rates agree with those acquired through levelling measurements made within investigation adit I and on surface for the time interval between 1997 and 2004, 2.1 to 2.5 ($\pm$0.03) cm/year. Thus more recent monitoring suggests that the movement has reduced since monitoring began in 1966 (Fig. 7c).

A similar conclusion can be reached when examining the temporal evolution of the triangulation targets installed on sliding mass E (Fig. 7d). The mean annual velocities for the period 1965/1974 to 2002, for targets 1320, 2103, 2135 and 2145 vary between 0.7 and 2.1 (±0.14) cm/year. In general, the trends of these targets show decreasing velocity with time suggesting a reduced interaction with the reservoir since the initial impounding.

## 7. Discussion

Many deep-seated rockslides, especially those involving shallow to moderately dipping rupture surfaces, characteristically demonstrate temporal variations in their measured slope velocities. Periods of acceleration are followed by periods of deceleration, both of which are heavily influenced by a combination of interacting causal and triggering mechanisms. Even though the variation in velocity between the phases of low and high slope activity can reach several orders of magnitude, sudden and rapid acceleration to failure is rarely observed.

In understanding these changing trends, the rockslide geometry has a major impact on the long-term deformation behaviour and stability of the slope and therefore needs to be defined in a reasonably accurate manner. This is best achieved through the integration and iterative analysis of data from geological and geomorphological surface mapping, subsurface in-situ investigations (boreholes, adits and geophysics), and deformation monitoring. Together, these measurements enable a kinematic model to be established.

The results of the investigations reported in this case study show that the Hochmais–Atemkopf rockslide system is comprised of several sliding masses arranged one on top of the other, with additional sliding masses developing side by side. On surface, each sliding mass could be identified and distinguished from the others based on mapped geological–geomorphological features (i.e. linear features, major scarps, etc.). These were in agreement with differential deformation patterns derived from geodetics, radar interferometry, etc. At depth, borehole core logs, seismic investigations, inclinometer profiles and deformation measurements from the investigation adit were used to locate sliding zones and slide boundaries.

However, despite the quality and quantity of data available, no rock slope data set is ever fully complete and some open questions remain that require further discussion and clarification. First, the available data does not allow a unique interpretation of whether the lower boundary of mass A daylights into the valley or passes under the valley floor. These two scenarios are illustrated in the cross section of Fig. 4, with each involving a different kinematic model with different hazard implications. The presence of a daylighting surface would suggest that the mass is kinematically free to move in a translational manner once progressive failure along the rupture surface reaches a critical threshold. In contrast, a deeper sliding surface below the valley floor would require a complex toe deformation mechanism before kinematic release would be possible. Data supporting the first scenario rely on high-precision levelling measurements along adit I where no slope deformations accept those of sliding mass D could be measured. The presence of steeply inclined E–W striking brittle fault zones in the investigation adit, which could define the northern boundary of the rockslide system, and the absence of movement of mass A since monitoring began (i.e. the main scarp is not active) also supports the latter hypothesis. In addition, experiences from other rockslides in the Gepatsch region would suggest that the basal sliding zone passes below the valley floor. Thus together the data more fully support the second of these two scenarios.

Similar uncertainty also exists for the location of the lower boundary of slide mass B given the absence of investigative boreholes drilled in the upper slope. The focus of the subsurface investigation on the lower slope enables alternative kinematic interpretations of the geometry of mass B. In the cross section presented (Fig. 4), the lower boundary of sliding mass B is defined primarily based on geological field mapping; i.e., the exposure of the main scarp and its relationship with the topography and surface deformation measurements. Together, the kinematic and geological models developed provide a basis for understanding deep-seated rockslides in similar anisotropic paragneisses, and in metamorphic crystalline rock masses in general. For example, at the neighbouring Kreuzkopf, it has been shown that the sliding zone is highly controlled by meso-scale discontinuities (Zangerl and Prager, 2008). Generally, the structurally induced rock mass anisotropy favours a planar translational failure mechanism rather than a classical rotational failure mode. Detailed analysis of the data for the Hochmais–Atemkopf rockslide system likewise suggests that the deformations for the different slide bodies generally concentrate along distinct sliding zones representing a translational sliding mechanism with only minor internal deformation of the sliding mass itself. This was clearly evident for sliding mass D (the Hochmais) in the adit levelling measurements and inclinometer measurements in borehole HM1. Direct measurements below this depth for the deeper slide bodies were limited by the 88 m depth of the HM1 inclinometer, which showed no internal deformation below mass D and the occurrence of an additional active sliding zone. Core logs extending deeper than the installed inclinometer, to 135 m, show several possible sliding zones composed of fractured and fragmentised paragneissic rock (i.e. fault gouge, breccias and cataclasites). Together these suggest en bloc movement of mass C and B.

The temporal behaviour of the rockslide system was likewise more fully established for sliding mass D than for the other sliding masses. To fully establish such behaviour, continuous or frequent displacement measurements with a precision of a few millimetres or less are required. Such precision is needed to resolve acceleration phases when the total displacements are less than a few centimetres per year. In this study, only the wire-line extensometer in the investigation adit I could reliably provide this level of resolution. The deformation data quality for sliding mass D was excellent with horizontal displacements measured with a resolution of 1 mm. Analysis of these displacements together with available hydrological data (i.e. reservoir level, flow rate of springs, etc.) showed that the velocity of sliding mass D was largely controlled by the fluctuating reservoir levels, and not periods of high and low precipitation on the slope. Although the initial filling of the reservoir immediately triggered acceleration of the Hochmais sliding mass, due to increasing water pressures and reduced effective stresses in the foot of the slope, subsequent intervals of acceleration were clearly attributed to the cyclic lowering of the reservoir level every year from late winter to early spring. Drawdown works to produce an increased hydraulic gradient within the slope, whereby the redistributed pore-water pressures together with increased seepage forces contribute to a disequilibrium condition and accelerating behaviour in the slide. Monitoring data shows these drawdown-induced velocities to be up to 1 mm per day, which are then reversed during the subsequent refilling of the reservoir, leading to deceleration of the slide mass.

Building on these results, and using them as a source of model constraint, hydromechanically coupled finite-element modelling is being undertaken by Schneider-Muntau et al. (2006a,b) to further study and understand the underlying mechanisms and provide insights into the different hazard scenarios with respect to uncertainties related to the nature of the different sliding masses. Results to date have been able to reproduce the temporal variable deformation pattern when reservoir level fluctuations are considered (i.e. high and low reservoir levels). These results will be published after the completion of the numerical modelling work providing further insights into the hydromechanically coupled slope deformation mechanisms for the Hochmais–Atemkopf rockslide system.

## 8. Conclusions

This paper reports the results of a detailed field-based investigation into the geometry, kinematics and temporal characteristics of a

prominent deep-seated rockslide system in paragneissic rock located above the Gepatsch hydroelectric reservoir in the inner Kaunertal, Tyrol, Austria. The results presented are part of an ongoing study and provide the basis for a series of hydromechanically coupled finite-element, visco-plastic creep models currently being carried out as part of the investigation. Results from the geological and geomorphological investigations, combined with subsurface *in-situ* investigations (boreholes, adits and geophysics), and deformation monitoring, indicate that the Hochmais–Atemkopf rockslide system involves several sliding masses, one on top of the other, characterized by different displacement patterns. Slope deformations are translational and concentrated along distinct sliding zones, with only minor internal creep deformation of the slide body rock mass in-between. The temporal characteristics of the most active sliding body, the Hochmais (also referred to as slide mass D), are clearly controlled by seasonal fluctuations in the reservoir level, with slope velocities peaking when the reservoir levels are at their lowest. It was found that the reservoir level as opposed to the rate of reservoir drawdown provides a better correlation with the intermittent accelerating behaviour of the rockslide.

## Acknowledgements

The authors wish to acknowledge and thank the Tiroler Wasserkraft AG (TIWAG), A-6020 Innsbruck for providing in-situ investigation and deformation monitoring data, and supporting this ongoing research project. Thanks are also extended to ILF Consulting Engineers Ltd., A-6063 Rum, p + w Baugrund + Wasser GEO-ZT GmbH, A-6060 Hall, alpECON Wilhelmy KEG, A-6165 Telfes, Kplus-FFG and Tiroler Zukunftsstiftung for supporting this work.

## References

Abele, G., 1974. Bergstürze in den Alpen. Ihre Verbreitung, Morphologie und Folgeerscheinungen. Wissenschaftliche Alpenvereinshefte Heft 25, München, 230 pp.

Azzoni, A., Chiesa, S., Frassoni, A., Govi, M., 1992. The Valpola landslide. Engineering Geology 33 (1), 59–70.

Bonzanigo, L., Eberhardt, E., Loew, S., 2007. Long-term investigation of a deep-seated creeping landslide in crystalline rock — geological and hydromechanical factors controlling the Campo Vallemaggia landslide. Canadian Geotechnical Journal 44 (10), 1157–1180.

Brideau, M.A., Stead, D., Kinakin, D., Fecova, K., 2005. Influence of tectonic structures on the Hope Slide, British Columbia, Canada. Engineering Geology 80 (3/4), 142–159.

Brückl, E., Zangerl, C., Tentschert, E., 2004. Geometry and deformation mechanisms of a deep seated gravitational creep in crystalline rocks. In: Schubert, W. (Ed.), Proceedings of the ISRM Regional Symposium EUROCK 2004 & 53rd Geomechanics Colloquium, pp. 229–230. Salzburg, Austria.

Brückl, E., Brunner, F.K., Kraus, K., 2006. Kinematics of a deep seated landslide derived from photogrammetric, GPS and geophysical data. Engineering Geology 88 (3/4), 149–159.

Crosta, G.B., Agliardi, F., 2002. How to obtain alert velocity thresholds for large rockslides. Physics and Chemistry of the Earth 27, 1557–1565.

Evers, H. 2006. Geodätisches Monitoring und einfache statistische Auswertungsmöglichkeiten für Massenbewegungen an Hängen. Master Thesis, HTWK Leipzig, p. 118.

Hammer, W., 1923. Österreichische Geologische Karte 1:75.000, Blatt Nauders, Nr. 5245.

Helmstetter, A., Sornette, D., Grasso, J.R., Andersen, J.V., Gluzman, S., Pisarenko, V., 2004. Slider block friction model for landslides: application to Vaiont and La Clapière landslides. Journal of Geophysical Research 109 (B02409), 1–15.

Hoinkes, G., Thöni, M., Bernhard, F., Kaindl, R., Lichem, C., Tropper, P., 1994. Pre-Alpine magmatic and metamorphic evolution of the Austroalpine Ötztal basement in the Kaunertal area. Mitteilungen der Österreichischen Mineralogischen Gesellschaft 139, 59–61.

Lauffer, H., Neuhauser, E., Schober, W., 1967. Uplift responsible for the slope movements during the filling of the Gepatsch reservoir. 9th International congress on large dams — (ICOLD), Istamboul, Turkey, Q. 32 R. 41, pp. 669–692.

Leobacher, A., Liegler, K., 1998. Langzeitkontrolle von Massenbewegungen der Stauraumhänge des Speichers Durlaßboden. Felsbau 16 (3), 184–193.

Noverraz, F., 1996. Sagging or deep-seated creep: fiction or reality? In: Senneset (Ed.), 7th International Symposium on Landslides. Balkema, Rotterdam, pp. 821–828.

Prager, C., Zangerl, C., Patzelt, G., Brandner, R., 2008. Age distribution of fossil landslides in the Tyrol (Austria) and its surrounding areas. Natural Hazards and Earth System Sciences 8, 377–407.

Rott, H., Scheuchl, B., Siegel, A., Grasemann, B., 1999. Monitoring very slow slope movements by means of SAR interferometry: a case study from a mass waste above a reservoir in the Ötztal Alps, Austria. Geophysical Research Letters 26 (11), 1629–1632.

Schneider-Muntau, B., Gerik, A., Zangerl, C., Fellin, W., 2006a. Hydromechanical coupled finite element modelling of a slowly creeping landslide. 3rd Colloquium Rock Mechanics — Theory and Practice, Vienna, Austria, Mitteilungen für Ingenieurgeolgie und Geomechanik, vol. 7, pp. 87–94.

Schneider-Muntau, B., Renk, D., Marcher, T., Fellin, W., 2006b. The importance of laboratory experiments in land-slide investigation. In: Nadim, F., Pöttler, R., Einstein, H., Klapperich, H., Kramer, S. (Eds.), Geohazards — Technical, Economical and Social Risk Evaluation, Lillehammer, Norwegen, ECI Symposium Series, vol. P7. http://services.bepress.com/eci/geohazards/12.

Tentschert, E., 1998. Das Langzeitverhalten der Sackungshänge im Speicher Gepatsch (Tirol, Österreich). Felsbau 16 (3), 194–200.

Weidner, S. 2000. Kinematik und Mechanismus tiefgreifender alpiner Hangdeformationen unter besonderer Berücksichtigung der hydrogeologischen Verhältnisse. Dissertation Thesis, Friedrich–Alexander Universität Erlangen–Nürnberg, 246 pp.

Zangerl, C., Eberhardt, E., Schönlaub, H., Anegg, J., 2007. Deformation behaviour of deep-seated rockslides in crystalline rock. In: Eberhardt, E., et al. (Ed.), Proceeding of the 1st Canada–U.S. Rock Mechanics Symposium, vol. 2, pp. 901–908. Vancouver, Canada.

Zangerl, C., Prager, C., 2008. Influence of geological structures on failure initiation, internal deformation and kinematics of rock slides. Proceeding of the 42nd U.S. Rock Mechanics Symposium / 2nd U.S.–Canada Rock Mechanics Symposium, San Francisco, ARMA 08-063, pp. 1–13.